

# Performance assessments of the SNPP and N20 VIIRS DNB using observations of bright stars.

Truman Wilson<sup>a</sup> and Xiaoxiong Xiong<sup>b</sup>

<sup>a</sup>Science Systems and Applications, Inc., 10210 Greenbelt Road, Lanham, MD 20706, USA;

<sup>b</sup>Sciences and Exploration Directorate, NASA/GSFC, Greenbelt, MD 20771, USA

## ABSTRACT

The Visible Infrared Imaging Radiometer Suite (VIIRS) on-board the Suomi-NPP (SNPP) and NOAA-20 (N20) spacecrafts is a multi-spectral Earth-observing instrument with spectral channels ranging from the visible to the long-wave infrared. In addition to these spectral channels, the VIIRS instrument features a panchromatic Day/Night band (DNB) with 3 gain stages (low, mid, and high) which allows for Earth-view (EV) radiance retrievals over 7 orders of magnitude. The DNB is able to collect data ranging from dim city lights during nighttime up to reflected sunlight from cloud-tops during daytime. The DNB data collection is divided into 32 aggregation modes, where sub-pixel aggregation is used to maintain a nearly constant pixel footprint on ground during EV data collection throughout each scan. The DNB is also sensitive enough to observe bright stars through the instrument space-view (SV) port. Data from these bright stars can be used to track the temporal stability of the sensor gain and as a method of intercomparison between the two VIIRS instruments. In this work, we will present several sensor performance assessments of the VIIRS DNB using stars. In addition to the sensor gain trending, these assessments will include a comparison of the differences between the daytime and nighttime data due to the effects of stray-light, a comparison of the measured signal as a function of aggregation mode, a comparison between the two high-gain sub-stages, and half-angle mirror side for both the SNPP and N20 VIIRS DNB.

**Keywords:** VIIRS, day/night band, calibration, stars

## 1. INTRODUCTION

The Visible Infrared Imaging Radiometer Suite (VIIRS) is a multi-spectral, whiskbroom scanning radiometer covering the wavelength range  $0.41 - 12.2 \mu\text{m}$ . The VIIRS instrument has been in operation on-board the Suomi National Polar-Orbiting Partnership (SNPP) and NOAA-20 (N20) spacecrafts since their launches in October 2011 and November 2017, respectively.<sup>1-3</sup> The VIIRS spectral channels include 14 Reflective Solar Bands (RSB), 7 Thermal Emissive Bands (TEB), and a pan-chromatic day/night band (DNB) with a wavelength range from 500 to 900 nm. A diagram of the VIIRS instrument can be seen in Figure 1(a). The VIIRS imagery is acquired through the use of a rotating telescope assembly (RTA), which rotates on an axis parallel to the direction of motion (track direction) to obtain image swaths perpendicular to the direction of motion (scan direction). The swath width for the Earth-view (EV) imagery is approximately 3060 km wide in the scan direction and 12 km wide in the track direction at nadir. The spectral bands are calibrated on orbit using a solar diffuser panel (SD) with its associated SD stability monitor (SDSM) for the RSB and DNB and a blackbody source (BB) for the TEB.<sup>1</sup> The background signal is obtained through views of deep space through the instrument space-view (SV) port, which is an extension of the EV port where the RTA can observe beyond the Earth-limb. Through the SV port, VIIRS can also observe the Moon, planets, and stars in order to perform additional sensor calibration and spatial registration assessments.<sup>4-8</sup> The lunar observations are performed on a near monthly basis and can be used to provide additional corrections to the calibration for the RSB.

The DNB (500 – 900 nm) is unique among the VIIRS spectral bands for its large dynamic range, which spans over 7 orders of magnitude. This allows for observations from faint city lights at night to the bright reflection of sunlight from cloud tops during the day.<sup>9,10</sup> To make this possible, the DNB operates using three gain stages, the

---

Further author information: (Send correspondence to T.W.)

T.W.: E-mail: truman.wilson@ssaihq.com, Telephone: 1 301 867 2120

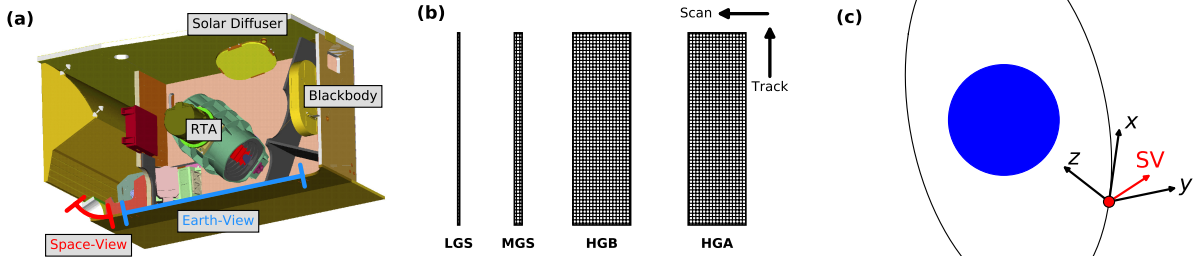


Figure 1. (a) Diagram of the VIIRS instrument. The SV port (red) is an extension of the EV port (blue). The RTA rotates on an axis parallel to the direction of the spacecraft motion. (b) Diagram of the FPA layout for the VIIRS DNB showing each gain stage. This diagram is not shown to scale. (c) Diagram of the VIIRS instrument coordinate system as it relates to the instrument orbit. The SV port is shown in red.

low- (LGS), mid- (MGS), and high-gain stages (HGS). The HGS is further split into two sub-stages designated as HGA and HGB. A diagram of the DNB gain stages on the focal plane assembly (FPA) is seen in Figure 1(b). The on-ground resolution of the DNB pixels is 750 m. However, whiskbroom sensors in low-Earth orbit are subject to the bow-tie effect in their imagery, which increases the size of the pixel footprint on ground away from nadir. To mitigate this, the DNB uses dynamic sub-pixel aggregation throughout the scan in order to create 16 effective detectors with near 750-m resolution throughout the entire scan. In the track direction, each gain stage has 672 sub-pixel detectors. In the scan direction, there are 1, 3, and 250 sub-pixel detectors for the LGS, MGS, and HGS, respectively. The aggregation occurs in 32 separate modes, with  $66 \times 42$  pixels aggregated for Aggregation Mode 1 (nadir) in the scan and track directions and  $11 \times 20$  for Aggregation Mode 32 (near the edge of scan).<sup>11</sup> However, for N20, a different aggregation option, Option 21 (Op21), was used in order to mitigate issues with non-linearity in some of the DNB aggregation modes.<sup>12–14</sup> Here, Aggregation Mode 21 is extended out to the edge of scan.

In the SV, the DNB is sensitive enough to observe bright stars, particularly in the HGS. In previous work, stars have been used to track the relative gain of the DNB on orbit, assess changes in the sensor relative spectral response (RSR) function, and as a method for intercomparison between the SNPP and N20 DNB HGS.<sup>5–7</sup> In this work, we will present a range of sensor performance assessments for the DNB using observations of stars. The coordinates and other properties of the stars that we will consider are taken from the Yale Bright Star Catalog (BSC).<sup>15</sup> In Section 2, we will present our methodology for identifying star observations in the DNB imagery and the spatial mapping of the DNB aggregation modes. In Section 3, we will discuss our data processing including the background subtraction method for stray light correction. In Section 4, we will show our sensor performance assessments, which will be split into subsections covering the gain trending, day/night comparisons, aggregation mode bias, HGA and HGB comparison, and the half-angle mirror (HAM)-side ratio. Finally, in Section 5, we will present our conclusions.

## 2. STAR IDENTIFICATION AND SPATIAL MAPPING

The DNB is able to observe a large number of stars over the SNPP and N20 orbital ranges, so positive identification of the correct star in the imagery will be necessary in order to make use of the data. In previous work, we showed how to predict the timing of star observations and identify the correct stars in the imagery.<sup>7</sup> We will review this methodology in this section.

It will be possible to view stars in the SV port only when the star is close the observation plane, which is the plane where the RTA rotates to view the various data sectors including the SV port. We consider the spacecraft coordinate system in a geodetic pointing configuration as follows. The  $z$ -axis points towards the normal of the ellipsoidal surface of the Earth at nadir. The  $x$ -axis is perpendicular to  $z$  and points in the direction of orbital motion. The  $y$ -axis is normal to the orbital plane. The observation plane in this case is defined as the  $yz$ -plane, and the SV port is located in this plane at  $24.325^\circ$  from the  $y$ -axis towards the  $z$ -axis. A diagram of the instrument coordinates can be seen in Figure 1(c).

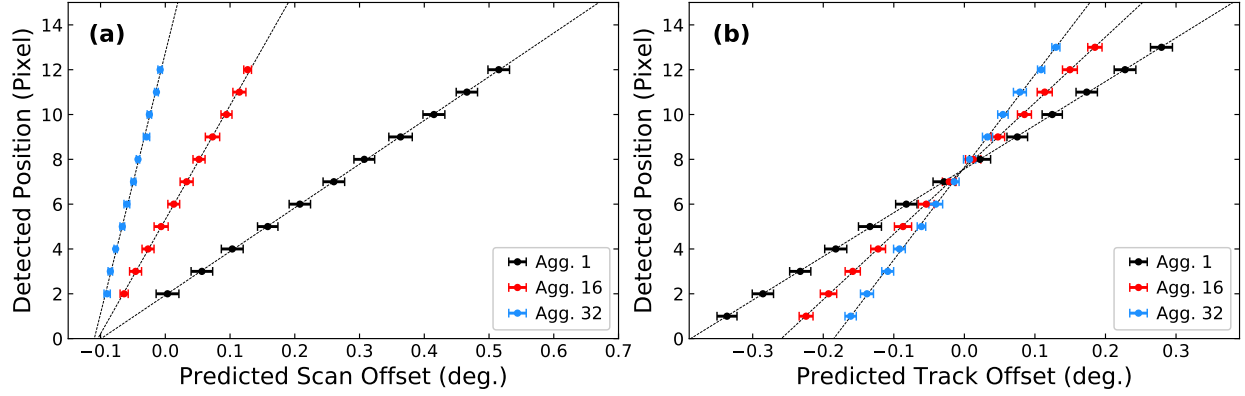


Figure 2. SNPP VIIRS DNB detected star positions versus the predicted angular offset of the star from the nominal SV port vector in the (a) scan direction and (b) track direction for selected stars. Each star detection is at an integer pixel number and the horizontal error bars show the standard deviations of the predicted angular offsets. The lower numbered aggregation modes have wider error bars because of the wider angular FOV per aggregated pixel.

Using spacecraft orbital data, we can predict the time when a target star crosses the  $yz$ -plane near the axis of the SV port.<sup>8</sup> For the RSB and TEB, the field-of-view (FOV) of the SV data sector is approximately  $0.9^\circ$  in both the scan and track directions. However, for the DNB, the SV sector FOV changes in a 72-scan cycle, where each of the 32 aggregation modes is used for each HAM side. An additional 4 calibration modes are also sampled for each HAM side to complete the cycle, but these modes are not used in the EV data.<sup>11</sup> For each aggregation mode, the FOV is different. Therefore, in order to accurately identify stars in the DNB imagery, we must first map the FOV of each aggregation mode in the SV port. This will allow us to distinguish between multiple stars in a single image and reject hot pixels caused by charged particle radiation which can resemble stars in the imagery. To do this, we select a subset of bright, isolated stars and measure the position of the peak pixel value when the star is expected to be close to the SV FOV as a function of the predicted angular offset from the SV port vector. Using a linear fit on this data in each aggregation mode in both the scan and track directions, we are then able to predict a star's location in the image when given an expected angular offset from the SV port. An example of this mapping for SNPP can be seen in Figure 2 for selected aggregation modes.

Using the fits from each aggregation mode, we can calculate the center and edge locations of each aggregation mode for both instruments, as seen in Figure 3. In the scan direction (Figure 3(a)), we see that each aggregation mode starts near the same value. The FOV then extends further for low number aggregation modes. For SNPP and N20, the FOV in the scan direction appears slightly offset likely due to a slightly different setting in the scan encoder values, which tells the instrument when to begin data collection for each sector. In the track direction (Figure 3(b)), the FOV is well centered for each aggregation mode about the SV port vector and shows good matching between the SNPP and N20 data. The N20 data is missing aggregation modes 22 – 31 since it uses Op21, as mentioned previously.

The coordinates of the stars in the BSC are given in celestial coordinates in terms of right-ascension and declination. The declination is defined as the angle above or below the celestial equator, which is the same plane as the Earth's equator. For SNPP and N20, we found that stars can be observed in the declination range from  $-15^\circ$  to  $32^\circ$ , over the full range of right-ascension.<sup>7,16</sup> Each star will typically be observed during two separate time frames throughout the year. The first observation typically occurs in the daytime part of the orbit, with the second observation occurring in the nighttime part of the orbit up to 7 weeks later depending on the star's declination. The stars can be visible for up to 10 scans per orbit for approximately 8 consecutive orbits. Throughout this work, we will refer to this time period where the star can be observed in successive orbits as an orbital cycle.

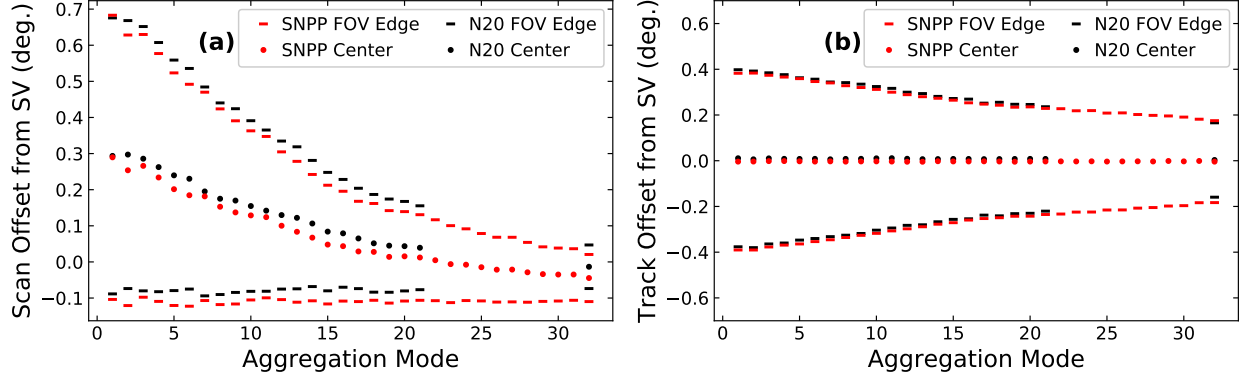


Figure 3. Angular FOV assessments for both SNPP and N20 in the (a) scan direction and (b) track direction. The dashes represent the edge of the FOV and the dots represent the center of the FOV as calculated from fits like those seen in Figure 2. For EV data, aggregation mode numbers start at 1 near nadir and increase going towards the edge of scan. The N20 data is missing aggregation modes 22 – 31 because it uses Op21 for pixel aggregation as described in Section 1.

### 3. DATA PROCESSING

With our star observation predictions and aggregation mode mapping, we are able to start processing data for each star. The first step in processing the imagery is to remove the background signal. For daytime images in particular, stray light contamination can cause the imagery to have a non-uniform background signal which cannot be removed by simply subtracting the lowest signal value for each aggregated detector.<sup>17</sup> To mitigate this issue, we developed an alternative method for background subtraction which is shown in Figure 4. First, we flatten the uncorrected data shown in Figure 4(a) by appending the values of each column in the image into a single column of data, represented by the black line in Figure 4(c). We fit a third order polynomial data to remove the trend while doing a  $3\sigma$  (3 standard deviations) outlier rejection in order to remove any potential star data from the trend. This results in the data represented by the blue line. Next, we reform the image and perform a detector level (for each row in the scan direction) background subtraction using the average of the lowest half of the pixel values in each row. Finally, we flatten the image by appending each row of data into a single column (transposed relative to the first step) and perform another polynomial fit subtraction. The final result is the data represented by the red line, and the image in Figure 4(b).

With the background-subtracted images, we perform several checks to ensure that the best data is used for our analyses. First, we use Laplacian of Gaussian Blob detection (Blob LoG) from Python’s *scikit-image* library

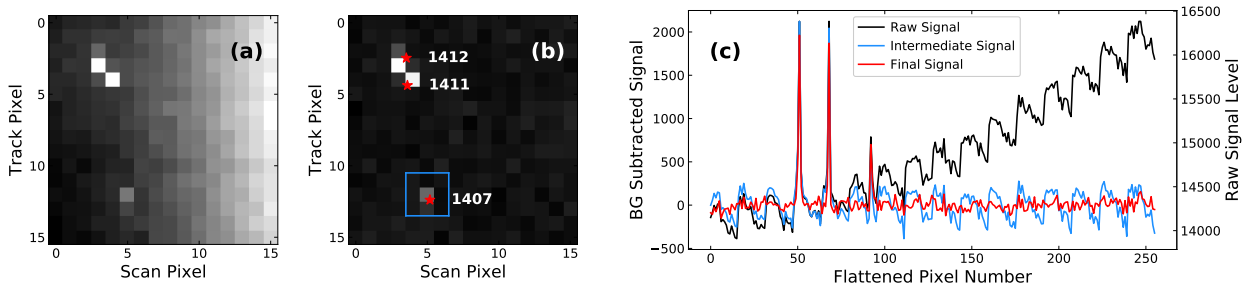


Figure 4. Example of the background subtraction methodology and star identification. (a) Raw image from SNPP in aggregation mode 4 during a daytime observation showing stray-light contamination at the right side of the image. (b) Background-subtracted image of (a). The red star symbols show the predicted location in the image of HR 1407, 1411, and 1412. The blue bounding box shows the  $3 \times 3$  integration region used in our calculations around HR 1407. (c) An example of our background subtraction methodology. The image is flattened and fit with polynomials both for the regular and transposed images. The blue intermediate signal line shows the subtraction after the first fitting.

to detect peaks in the images.<sup>18</sup> We require that the detections in both HGA and HGB are within 1 pixel of each other in order to remove hot pixels that appear in just one of the images. Next, we use the mapping to predict the locations of the stars in the image, as seen in Figure 4(b), and require that the detected and predicted positions are within 1.2 pixels of each other to allow a buffer for spacecraft attitude offsets. Finally, we require that the nearest neighbor star must be at least 2 pixels away, in order to ensure that it does not add unwanted background signal to the  $3 \times 3$  integration region that will be used to obtain the final signal (blue square in Figure 4(b)). In the case of Figure 4(b), the observation for HR 1407 would be used in our data, whereas those for HR 1411 and 1412 would be rejected.

For each image, we extract a  $3 \times 3$  sub-image around the star and integrate it to calculate the total signal level,  $dn$ . We can calculate the irradiance of the star in the image,  $L_*$ , by using gain and solid angle correction factors as seen in the following equation:

$$L_* = dn \cdot F \cdot c \cdot \frac{p_{sc} \cdot p_{tr}}{h^2} \quad (1)$$

Here,  $F$ , is the SD F-factor which is used to track the change in the on-orbit gain throughout the mission,  $c$  is the calibration coefficient (for the DNB, only the linear calibration coefficient is used from what is typically a 3rd order polynomial with respect to  $dn$ ), and the  $p_{sc} \cdot p_{tr} / h^2$  term represents the solid angle correction. Here,  $p_{sc}$  and  $p_{tr}$  are the pixel size in the scan and track directions on ground if the view were at nadir, and  $h$  is the nominal altitude of the spacecraft, which is 824 km. The  $F$ ,  $c$ , and  $p$  terms are all aggregation mode dependent, with the F-factor also being time-dependent. The  $F$  and  $c$  values are provided by the NASA VIIRS Characterization Support Team (VCST).<sup>19</sup> For the HGS, the F-factor is derived from the SD data via the LGS and MGS using a ratio approach. This is because HGS data saturates when the SD is fully illuminated by the sun. However, for the assessments discussed in Section 4, the pre-launch (PL) F-factor will be used primarily so we can assess the change in the sensor gain over time. Both  $F$  and  $c$  are provided as the average between HGA and HGB for the HGS.

## 4. SENSOR PERFORMANCE ASSESSMENTS

### 4.1 Sensor Gain Trending

With the ability to identify star observations accurately, we are ready to analyze the on-orbit performance of the sensor. The first assessment we perform is for the on-orbit gain of the sensor. For on-orbit operations, the gain of the DNB is measured by the SD and is represented by the inverse of the F-factor. While the SD F-factor is measured for each aggregation mode, for star measurements, the observations for each orbit will sample only a small subset of the aggregation modes. In order to analyze the star data in this work, we will average each set of observations for a given star over the full orbital cycle and compare to the band-averaged gain derived from the SD. Since the data from daytime observations is impacted by stray light (see Section 4.2), the observations used here will be limited to nighttime observations. An example of this data averaging can be seen in Figure 5(a). For this data, the gain correction factors discussed above are applied to each individual measurement before the averaging is performed using both PL F-factors and those derived on-orbit from the SD data. For this work, correction factors for the on-orbit RSR change are not included.<sup>20</sup> These impacts are the subject of ongoing work. However, for K-type stars (more "red" than the Sun, a G-type star), the magnitude of the modulated-RSR impact is small compared to other stellar temperature classes since the stellar spectra of these stars is broad over the RSR range of the VIIRS DNB.<sup>7</sup> In the data averaging for each orbital cycle, we use a  $3\sigma$  outlier rejection to remove data points that are far from the center of the distribution.

Since accurate absolute spectral irradiance data is not readily available for most of the stars where we have observations, we need to normalize the data from each star in order to account for differences in the brightness. Since the stars are only observable for short periods of time throughout the year and because the DNB gain for SNPP changes rapidly during the first year of the mission, a simple normalization to the first data point for each star is not recommended. As seen in Figure 5(a), the PL data (black data) can have a large discontinuity between the first two orbit cycles. While applying the SD F-factor to the data (red data) does not remove all of the trend, it does remove enough to allow us to use a linear fit to extrapolate the data back to a common

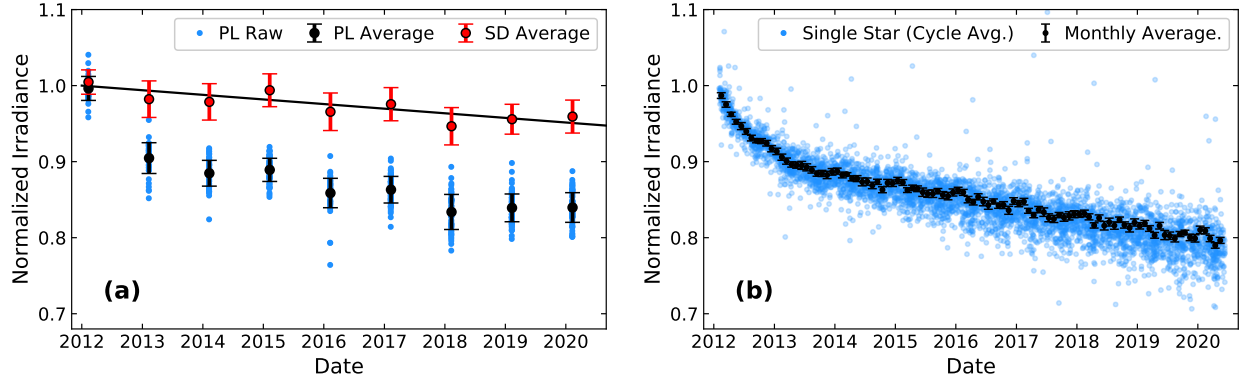


Figure 5. Example gain trending calculation for SNPP. (a) The blue dots represent the individual (scan level) measurements for HR 1084 (K-type star) with the pre-launch calibration coefficients applied. The black data shows the average for each orbital cycle, with the error bars representing the standard deviation of the measurements. The red data shows the application of the SD F-factor to the black data, with a corresponding linear fit used for data normalization. (b) Gain trending using combined data from all K-type stars after normalization. The blue data shows all of the cycle-averaged PL data for each star. The black data uses a weighted averaged of the data for each month, with error bars propagated from the individual measurements.

reference point (January 1, 2012/2018 for SNPP/N20). This value can then be used to rescale the data for each star relative to this common reference point. Applying these scaling factors to the prelaunch data will allow us to derive the band-averaged gain trending as shown for SNPP in Figure 5(b) using K-type stars. Since we have a large number of star observations, we can group the data each month using a weighted-averaged with a  $3\sigma$  outlier rejection. The final data is shown in black in Figure 5(b), with error bars propagated from the standard deviation of the cycle-averaged data.

In Figure 6, we show a comparison of the band-averaged SD gain for the DNB HGS with the star data for both SNPP and N20. For both instruments, the star data shows more degradation compared to the SD data. This SD data is derived using a ratio approach with HGS and MGS data.<sup>19</sup> The star data shown here might allow us to provide a correction to the HGS data similar to how lunar data is used to provide a correction to the other RSB.<sup>4</sup> In addition to the gain trending data, analyzing data from different spectral classes will allow us to assess the change in the RSR over the course of each mission. For SNPP in particular, the DNB sensitivity at long wavelengths decreased relative to the sensitivity at shorter wavelengths.<sup>20</sup> With our improved methodology for deriving the trending gain, we are able to achieve much greater signal-to-noise levels in the star data compared to previous work.<sup>5,6</sup> This will allow us to distinguish between the trends of stars of different spectral classes. If we look at A/B-type stars (blue) compared to K-type stars (red), we can see that the gain trending from the K-type stars diverges early in the mission from the A/B-type stars, trending lower as expected. After 2014, the difference appears more stable. For N20, there is no apparent difference between the two datasets. A full analysis of the modulated-RSR in the DNB using stars is the subject of on going work.

## 4.2 Stray Light and Day/Night Differences

The data analyzed in the previous sections has used nighttime data in order to make the comparisons. This is because of the significant stray-light impact in the imagery that occurs during spacecraft daytime as shown in Figure 4. While the technique illustrated previously to remove the stray-light provides an improvement to the daytime data, the daytime data remains more noisy than the corresponding nighttime data for a given star. In Figure 7 we show a comparison of daytime and nighttime observations for K-type stars for both instruments. Here, daytime data is derived only for stars that have a corresponding nighttime orbital cycle. The scale factors are derived from nighttime data as shown in Figure 5 and applied to both daytime and nighttime data for a given star. For both SNPP and N20, the daytime data is noisier compared to the nighttime data and has a larger uncertainty. For the daytime data, much of the data for low aggregation modes is lost since the stray light can cause saturation of the HGS pixels. For some stars, we end up with only a few observations per orbital

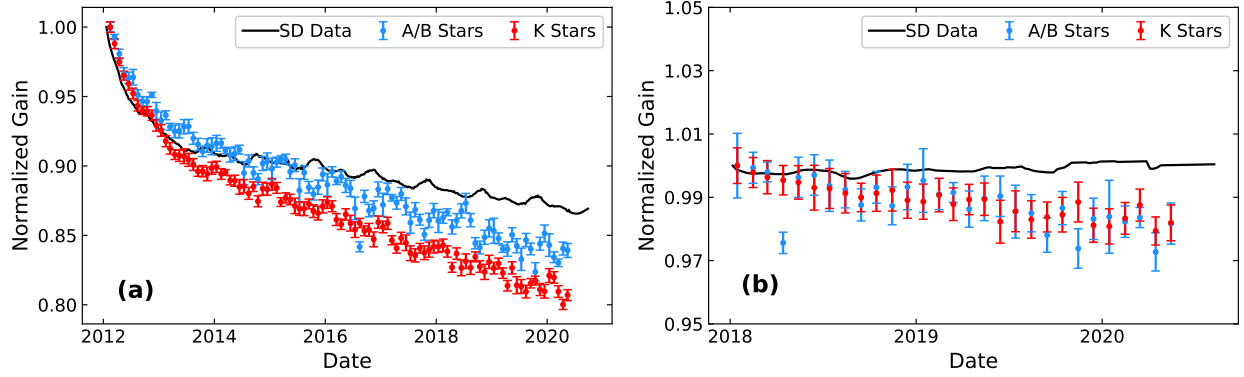


Figure 6. Trending gain comparison with the SD F-factor for (a) SNPP and (b) N20. In each case, data for A/B-type stars is shown along with data from K-type stars. The SD data is averaged over all aggregation modes.

cycle which can adversely impact the data. For this comparison, we require that any data point has at least 5 observations within the orbital cycle to ensure reasonable data sampling.

For the SNPP data, the daytime and nighttime trends and magnitude match well early in the mission. In 2014, we see that the data starts to diverge, with the daytime data showing a slightly higher measured value compare to the nighttime data. The cause of this divergence is currently unknown, but there are a few potential causes that need to be investigated. First, since the gain decreases over time, the amount of saturation in the images decreases which may lead to a larger number of high stray light images being included. While there may be less saturation, the stray light for those images will be more difficult to remove and may cause a positive bias in the data through the inclusion of additional unremoved background signal. Second, the daytime data trends closer to the derived SD gain trending which also takes place during spacecraft daytime, which might imply some difference in the gain between day and night time data. For N20, there is not a significant difference between daytime and nighttime data. However, the increase in the noise level of the daytime data tends to mask any trend that might exist in the data. For the nighttime data shown in Figure 6(b), a clear downward trend is shown in the star data, whereas no clear trend can be extracted from the daytime data.

### 4.3 Aggregation Mode Comparison

For the next assessment, we will split the data by aggregation mode and compare the relative bias. In this case, we will not look at the time series of the data but instead look at the bias averaged through the entire mission for K-type stars. For this assessment, we will look at the integrated, background-subtracted signal without any

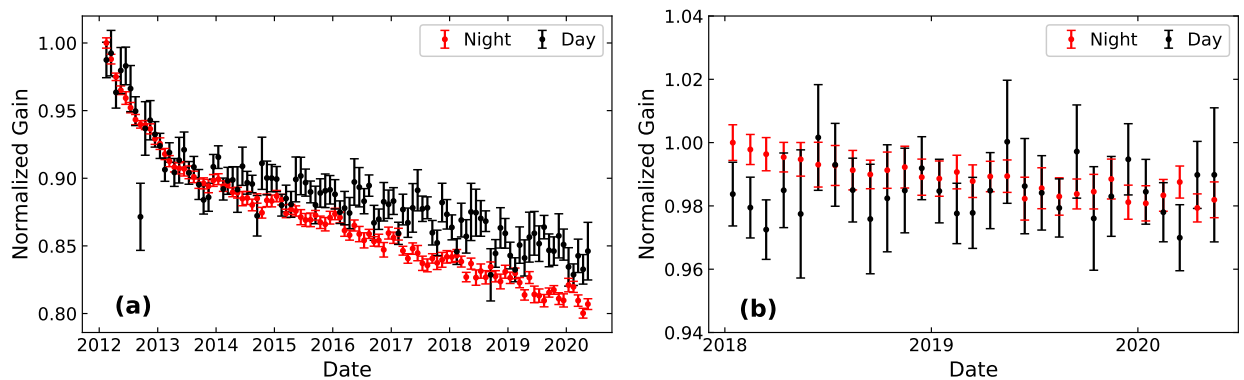


Figure 7. Trending gain comparison between daytime and nighttime star observations for (a) SNPP and (b) N20. This comparison uses K-type stars for both instruments.

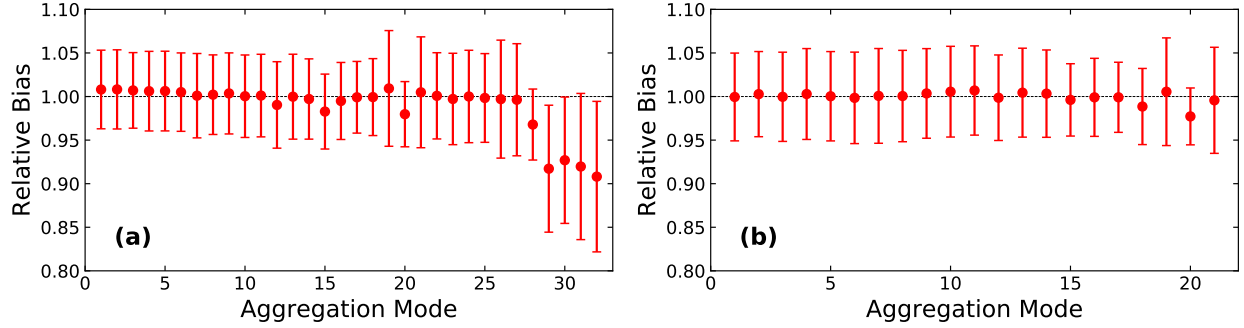


Figure 8. Relative bias in the measurements as a function of aggregation mode for (a) SNPP and (b) N20. For N20, aggregation modes above 21 are not considered for this plot due to the use of Op21 discussed in the text. The error bars in the plot show the standard deviation of the bias for each aggregation mode.

aggregation mode dependent SD F-factors applied. This will allow us to assess the signal response difference from the aggregation modes without any potential bias introduced from the SD F-factors. To do this, we first rescale the data for each star to account for differences in brightness using fits as we did in Figure 5(a). We then remove the mission long band-averaged gain trending using a spline fit to the gain data seen in Figure 5(b). With the gain and brightness variation removed from the data, we can then compare the data for each aggregation mode to the mean. The results for this calculation are seen in Figure 8 for both instruments. In each instrument, the results are consistent across the higher FOV aggregation modes (low aggregation mode number), with a bias less than 1% for most modes. At high aggregation mode numbers for SNPP the signal level appears to show a sharp decrease. The source for this discrepancy is not clear but there are a number of possibilities that we will pursue moving forward. First, it's possible that the solid angle correction factors shown in Equation 1 need an adjustment to correct for the actual FOV size. The current factors as based on the number of pixels used in the scan and track directions for each aggregation mode, as pre-launch measurements of the FOV are only available for a few aggregation modes. Another possibility is that the modulation transfer function (MTF) of the system spreads the light out across more than the  $3 \times 3$  pixel region, which would cause a decrease in the signal for lower FOV aggregation modes as some light from the star might be cut off. Since stars are nominally point sources as seen by the sensor, they make a good candidate for an MTF measurement source for the DNB. This possibility will need to be explored further in the future.

#### 4.4 Comparison of High-Gain A to High-Gain B

Data for the DNB HGS uses the average of the two sub-stages during the EV retrieval. In principle, these two sub-stages could show diverging behavior on orbit. If this were the case, then it could be beneficial to prioritize the data from one sub-stage over the other in on-orbit operations if one were to show anomalous behavior. The data from the SV sector separates the signal from HGA and HGB so that we are able to do a comparison of the measured signal using data from stars. To do this, we first group the data from all observations each month throughout the respective missions. Here, we combine the data from all spectral types since any spectral correction would be common to both gain stages. We then perform a linear fit to the HGA versus HGB data. The slope of the fit gives us our HGB/HBA ratio, as seen in Figure 9. For the SNPP data shown in Figure 9(a), there is an apparent bias in the data of approximately 0.3%, which is stable throughout the mission. For N20 VIIRS, the data appears slightly more noisy than what we observe for SNPP, but with a ratio that is near unity. SNPP also showed noisier behavior early in the mission but has since settled up to the present date. We will continue to monitor the N20 data to see if this behavior continues.

#### 4.5 Half-Angle Mirror Side Ratio

For the SD F-factor data, the HGS F-factor is derived using a ratio approach with data from the LGS and MGS. The derived look-up-tables for the HGS use a similar formulation, with a base level gain derived from the LGS with an addition scaling factor to apply to retrieve the HGS gain correction. Since the HAM exists

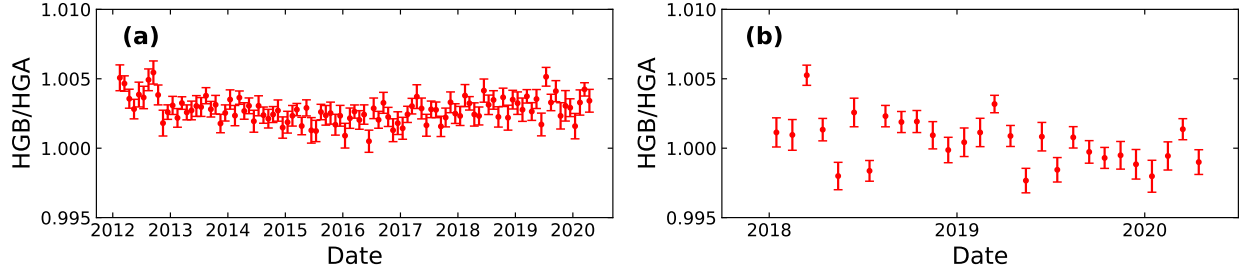


Figure 9. HGB to HGA ratio measurements for (a) SNPP and (b) N20. The data is grouped for each month and the ratio is found using the slope of a linear fit of the data.

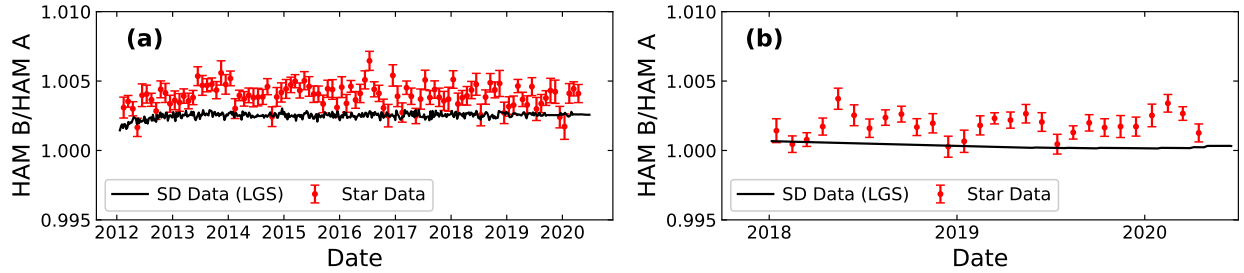


Figure 10. HAM-B to HAM-A ratio measurements for (a) SNPP and (b) N20. The data is grouped for each month and the ratio is found using the slope of a linear fit of the data. The black lines show the HAM side ratio derived from the SD LGS.

separately from the sensor array, the HAM-side dependence should not be dependent on the gain stage. In the look-up-tables provided by VCST, the HAM-side dependence only exists in the LGS data. Using star data, we can make an independent assessment of the HAM-side ratio which we can compare to the data derived from the SD. In Figure 10, we show the results for both instruments. The data is derived in the same fashion as the HGB/HGA ratio discussed previously. For each instrument, we see a small bias between the HGS data from our star measurements and the HAM-side ratio derived from the SD. In the case of SNPP, both sets of data show a similar trend, with a slight increase in the ratio early in the mission which is stable afterwards. For N20, both trends are relatively flat.

## 5. CONCLUSION

In this work, we showed the development of our methodology for using stars to assess the sensor performance of the VIIRS DNB HGS. These assessments will be beneficial for continued monitoring of the on-orbit performance of the VIIRS DNB and included the sensor gain trending, daytime versus nighttime comparisons, aggregation mode bias, HGB/HGA ratio and HAM-side ratio. To make this possible, we developed methodology to use bright, isolated stars in order to accurately map out the FOV of each aggregation mode which allows us to track and identify stars in the imagery. We also showed our methodology for removing the non-uniform background signal seen in the imagery associated with stray light contamination for observations that take place during spacecraft daytime. To monitor the gain trending, we average the data for each star over their respective orbital cycles and scale the data by extrapolating to a common reference point. This produced a trend which we could compare to the SD data. The star data shows around a 7% greater reduction in signal over the course of the mission using data from K-type stars compared to the SD. This data also showed a separation in the trending gain from blue stars (A/B-type) and red stars (K-type) which can be attributed to the change in the sensor spectral response for SNPP. For N20, the data showed no such discrepancy. For the other performance assessments, we showed that nighttime data was of higher quality than daytime data, which is impacted by stray light for both instruments. We also showed a slight bias in the signal for low number (high FOV) aggregation modes in each

instrument. The ratio between the two gain stages, HGA and HGB, and HAM sides were stable throughout each mission.

In the future, we will work to further understand the differences that we see in the gain trending when compared to the SD data. Also, we will investigate the impact of applying the modulated-RSR correction to the discrepancy in the trending between blue and red stars. We will also look at improving our background subtraction methodology further in order to improve the quality of the daytime data to the level of the nighttime data. As more VIIRS instruments are put into on-orbit operations over the coming years, star observations will prove to be an invaluable tool for characterizing the performance of the DNB HGS.

## ACKNOWLEDGMENTS

The authors would like to acknowledge the contributions from the VIIRS Characterization Support Team (VCST) for their valuable insights into the operations of the VIIRS instrument. In particular we would like to thank Chengbo Sun and Hongda Chen of VCST for providing the on-orbit SD F-factors for the VIIRS DNB. We would also like to thank Graziela Keller (formerly of VCST, currently at NASA JPL) for all of her valuable insights and discussions during the earliest portions of this work. Finally, we would like to thank Kevin Vermeesch of GST for his review of this manuscript.

## REFERENCES

- [1] Xiong, X., Butler, J., Chiang, K., Efremova, B., Fulbright, J., Lei, N., McIntire, J., Oudrari, H., Sun, J., Wang, Z., and Wu, A., “VIIRS on-orbit calibration methodology and performance,” *J. Geophys. Res. Atmos.* **119**, 5065–5078 (2014).
- [2] Cao, C., Deluccia, F., Xiong, X., Wolfe, R., and Weng, F., “Early on-orbit performance of the Visible Infrared Imaging Radiometer Suite (VIIRS) onboard the Suomi National Polar-Orbiting Partnership (S-NPP) satellite,” *IEEE Trans. Geosci. Rem. Sens.* **52**(2), 1142–1156 (2014).
- [3] Xiong, X., Cao, C., Lei, N., Chiang, K., Angal, A., Li, Y., Blonski, S., Wang, W., and Choi, T., “Early results from NOAA-20 (JPSS-1) VIIRS on-orbit calibration and characterization,” *Proc. IGARSS* **2018**, 1112–1115 (2018).
- [4] Xiong, X., Sun, J., Fulbright, J., Wang, Z., and Butler, J., “Lunar calibration and performance for S-NPP VIIRS reflective solar bands,” *IEEE Trans. Geosci. Rem. Sens.* **54**(2), 1052–1061 (2015).
- [5] Xiong, X., Wilson, T., Angal, A., and Sun, J., “Using the moon and stars for VIIRS day/night band on-orbit calibration,” *Proc. SPIE* **11151**, 11151Q (2019).
- [6] Fulbright, J. and Xiong, X., “Suomi-NPP VIIRS day/night band calibration with stars,” *Proc. SPIE* **9607**, 96071S (2015).
- [7] Wilson, T. and Xiong, X., “Intercomparison of the SNPP and NOAA-20 VIIRS DNB high-gain stage using observations of bright stars,” *IEEE Trans. Geosci. Rem. Sens.* (2020).
- [8] Wilson, T. and Xiong, X., “Planning lunar observations for satellite missions in low-earth orbit,” *J. Appl. Remote Sens.* **13**(2), 024513 (2019).
- [9] Liao, L. B., Weiss, S., Mills, S., and Hauss, B., “Suomi NPP viirs day-night band on-orbit performance,” *J. Geophys. Res. Atmos.* **118**, 12,705–12,718 (2013).
- [10] Román *et. al.*, M., “NASA’s black marble nighttime lights product suite,” *Remote Sens. of Env.* **210**, 113–143 (2018).
- [11] ATBD, VIIRS GEO, “Joint polar satellite system (JPSS) visible infrared imaging radiometer suite (VIIRS) sensor data record (SDR) geolocation algorithm theoretical basis document (ATBD),” (2013).
- [12] Oudrari, H., McIntire, J., Xiong, X., Butler, J., Efremova, B., Ji, J., , Lee, S., and Schwarting, T., “JPSS-1 VIIRS pre-launch radiometric performance,” *Proc. SPIE* **9607**, 960710 (2015).
- [13] Wang, W. and Cao, C., “NOAA-20 VIIRS DNB aggregation mode-change: prelaunch efforts and on-orbit verification/validation results,” *IEEE J. of Sel. Topics in Appl. Earth Obs. and Rem. Sens.* **12**(7), 2015–2023 (2019).

- [14] Schwarting, T., McIntire, J., Oudrari, H., and Xiong, X., “JPSS-1/NOAA-20 VIIRS day-night band prelaunch radiometric calibration and performance,” *IEEE Trans. Geosci. Rem. Sens.* **57**(10), 7534–7546 (2019).
- [15] Hoeffleit, D. and Jaschek, C., [*The Bright Star Catalog, 5th rev. ed.*], New Haven, CT, USA: Yale University Observatory (1991).
- [16] Wilson, T. and Xiong, X., “Scheduling observations of celestial objects for earth observing sensor calibration,” *Proc. SPIE* **10000**, 1000011 (2016).
- [17] Sun, C., Schwarting, T., Geng, X., Chiang, K., Chen, H., and Xiong, X., “VIIRS DNB time-dependent stray light correction,” *Proc. SPIE* **11127**, 111271W (2019).
- [18] van der Walt, S., Schönberger, J. L., Nunez-Iglesias, J., Boulogne, F., Warner, J. D., Yager, N., Gouillart, E., Yu, T., and the scikit-image contributors, “scikit-image: image processing in Python,” *PeerJ* **2**, e453 (6 2014).
- [19] Chen, H., Xiong, X., Sun, C., Chen, X., and Chiang, K., “Suomi-NPP VIIRS daynight band on-orbit calibration and performance,” *J. Appl. Remote Sens.* **11**(3), 036019 (2017).
- [20] Lei, N., Xiong, X., and Guenther, B., “Modeling the detector radiometric gains of the Suomi NPP VIIRS reflective solar bands,” *IEEE Trans. Geosci. Rem. Sens.* **53**(3), 1565 (2015).